Final Draft
of the original manuscript:

Srinivasan, P.B.; Liang, J.; Blawert, C.; Stoermer, M.; Dietzel, W.:
Effect of current density on the microstructure, corrosion behaviour of plasma electrolytic oxidation treated AM50 magnesium alloy
In: Applied Surface Science (2008) Elsevier

DOI: 10.1016/j.apsusc.2008.11.008

Effect of current density on the microstructure and corrosion behaviour of plasma electrolytic oxidation treated AM50 magnesium alloy

P. Bala Srinivasan*, J. Liang, C. Blawert, M. Störmer, W. Dietzel
Institute of Materials Research
GKSS-Forschungszentrum Geesthacht GmbH
D 21502 Geesthacht, Germany

*Corresponding Author (bala.srinivasan@gkss.de);
Phone: 00-49-4152-871997; Fax: 00-49-4152-871909

Key words
Magnesium alloy; Plasma electrolytic oxidation; Microstructure; Surface roughness; Thickness; Corrosion resistance.

*Corresponding Author (bala.srinivasan@gkss.de)

Abstract

Plasma electrolytic oxidation (PEO) of an AM50 magnesium alloy was accomplished in a silicate based electrolyte using a DC power source. Coatings were produced at three current densities i.e. 15 $mA{\cdot}cm^{-2}$, 75 $mA{\cdot}cm^{-2}$, 150 $mA{\cdot}cm^{-2}$ and were characterised for thickness, roughness, microstructural morphology, phase composition, and corrosion resistance. Even though the 15 minutes treated coatings produced at higher current density levels were thicker, they showed poor corrosion resistance when compared to that of the coatings obtained at 15 $mA{\cdot}cm^{-2}$. Short term treatments (2 minutes and 5 minutes) at 150 $mA{\cdot}cm^{-2}$ yielded coatings of thickness and corrosion resistance comparable to that of the low current density coatings. The superior corrosion resistance of the low thickness coatings is attributed to the better pore morphology and compactness of the layer.

Introduction

Corrosion protection of magnesium alloys is contemplated by many ways of surface treatments such as anodizing, plating, vapour deposition, polymer coatings etc. [1-5]. Even though each treatment has its own unique advantage, plasma anodization treatments have become increasingly popular for magnesium alloys owing to the process flexibility and environmental friendliness [6]. The plasma electrolytic oxidation (PEO), also known as micro arc oxidation, is carried out in general in aqueous alkaline electrolytes to develop ceramic coatings on the surface for the required protection [7-9].

A large number of publications have addressed the effect of electrolytes on the composition of coating and resultant properties [10-12]. Liang et al., have studied the effect of wave forms of current density on the formation of coating during micro arc oxidation of AM60B alloy in a silicate electrolyte [13] and Timoshenko et al., have made investigations on the PEO processing under pulse polarization modes [14].

Current density plays an important role in electrochemical treatments, and in this work an attempt has been made to understand the effect of this parameter on the evolution and the resultant properties of the coatings. PEO treatments were performed in a silicate based electrolyte at three different current density levels and the coatings were characterised for their microstructural features and corrosion behaviour. Based on the initial experiments, the effect of short duration treatments on the properties of coatings was also studied in this investigation.

Experimental

A cast magnesium alloy corresponding to AM50 with a nominal composition of 5% Al and 0.5% Mn was used in this investigation. Specimens of size 15 mm x 15 mm x 5 mm were polished successively up to 2500 grit emery finish and cleaned with acetone before the PEO treatment. The PEO electrolyte consisted of 10 g of potassium hydroxide and 10 g of sodium silicate in 1 liter of distilled water. The treatments were performed at three different current densities i.e. 15 $mA{\cdot}cm^{-2}$, 75 $mA{\cdot}cm^{-2}$ and 150 $mA{\cdot}cm^{-2}$ using a DC power supply of 600V / 4A capacity, and the specimens are referred to as A, B and C, respectively in the following sections.

The thickness of the coatings was assessed using MiniTest 2100 meter. Surface roughness measurements were carried out with a Hommel profilometer. Thickness measurements were made at 10 different locations and 4 scans were made for assessment of roughness on all specimens. Specimens for the microstructural examination (cross-section) were prepared by polishing successively using 500, 1200 and 2500 grit emery sheets, followed by final disc polishing using colloidal silica suspension OP-S. The phase composition analysis was done in a Bruker X-ray diffractometer with Cu-Kα radiation.

The corrosion potentials of the specimens were measured for a period of 1800 s before performing the electrochemical tests using a Gill AC potentiostat/galvanostat FRA

system which was employed for the corrosion studies. Electrochemical impedance spectroscopy (EIS) was performed using a three electrode cell, with 10 mV applied amplitude in the frequency range 0.01 Hz to 30,000 Hz at the free corrosion potential. Potentiodynamic polarisation studies were carried out at a sweep rate of 0.5 $mV \cdot s^{-1}$ starting at -200 mV relative to the open circuit potential and the experiments were continued up to a final current density of 1 $mA \cdot cm^{-2}$. The uncoated specimens were prepared by polishing up to 2500 grit emery for the electrochemical studies, while the PEO coated specimens were used in the as-coated condition. Experiments were performed at ambient temperature (21 $\pm$ 2°C) in non-deaerated 0.1 M NaCl solution in the as-prepared condition (pH ~6.5).

Results and Discussion

Evolution of coating

The physical changes that occurred on the surface of the magnesium alloy substrate during the evolution of coating in the PEO process was monitored by visual observation and by measurement of voltage as a function of time. Even though the publications of Lv et al., **(15-16)** have addressed the PEO process of magnesium alloys in only two stages, it is appropriate to discuss the coating formation in four stages. The different stages are marked in the voltage vs. time plots obtained at various current densities and presented in **Figure 1**. The first stage was marked by a rapid increase in voltage with the dissolution of magnesium alloy substrate and the associated passive film formation on the surface. Very fine sized discharges of milk-white colour began to appear at a voltage termed as breakdown potential (225 $\pm$ 10 V in this electrolyte) marking the onset of the second stage which continued up to a point (around 380 V) where a change in colour of sparks from white to orange/red was observed. In the third stage, the sparks started to grow in size, in addition to their changing colours, and the rate of increase in voltage dropped drastically in this region. In the last stage, the sparks grew still bigger in size, and the spark density on the surface came down significantly. It should be pointed out here that not all the sparks were bigger and there existed a few fine sparks as well until the end of the process. It was observed that at the higher current density levels, too, the voltages marking the various stages remained the same (within $\pm$ 10 V) as that of the 15 $mA \cdot cm^{-2}$ case. However, these stages were attained much faster in the 75 $mA \cdot cm^{-2}$ and even quicker in the 150 $mA \cdot cm^{-2}$ conditions. Further, the large sparks observed in the 4^{th} stage were long lived compared to those observed in the earlier stages.

Microstructure and morphology

The scanning electron micrographs showing the cross-section of the PEO coated specimens at different current densities are presented in **Figure 2**. All the coatings were observed to have a wavy-jagged interface with the substrate, which is most likely as a result of the dissolution of the substrate in the early stage of treatment. The coating obtained at the low current density level was more compact and the coatings produced at higher current density levels had a higher degree of micro-cracks. The development of such defects in the PEO coatings is attributed to the thermal stresses during the evolution of coating as a result of melting and solidification of hard ceramic compounds such as magnesium oxide, magnesium silicate, etc. The average energy input values were approximately 6 $W{\cdot}cm^{-2}$, 34 $W{\cdot}cm^{-2}$ and 78 $W{\cdot}cm^{-2}$, for the low, intermediate and high current density operations. The higher energy input and the resultant higher thickness of coatings in the high current density operations were also responsible for such appearance. It is also to be noted that the pore channels originating from the surface seem to be interconnected and go down to the substrate in these two coatings (marked by arrows in Figures 2(b) and 2(c)).

The surface morphologies of the PEO coated specimens are shown in **Figure 3**. In the specimen A-15 treated at 15 $mA{\cdot}cm^{-2}$ pores of three different size ranges (1 ± 0.5 μm, 4 ± 1 μm and 8 ± 2 μm in diameter) are evident. In the specimens processed at higher current density levels, the number of pores (pore density) seems to have come down; however, the sizes of the pores are quite large. This is in agreement with the qualitative visual observations on the spark density made during the coating evolution. In specimens B-15 and C-15 one could observe large chunks of oxide coating, which is on account of the higher energy input and associated large spark sizes. In addition, the presence of micro-cracks on the surface of these specimens is also evident in micrographs 3b and 3c.

Roughness, Thickness and Phase composition

The average thickness and surface roughness values of the PEO coated specimens are presented in **Figure 4**. The influence of current density on the coating thickness was profound, and the coating obtained at 150 $mA{\cdot}cm^{-2}$ was three times thicker than that of the coating produced at 15 $mA{\cdot}cm^{-2}$. The roughness values of the coatings were also found to be higher with increase in current density. The formation of oxide coating as large chunks at higher current density levels and the large pore sizes are responsible for the increased surface roughness.

The X-ray diffraction patterns for the three PEO coated specimens are shown in **Figure 5**. In all the three cases peaks corresponding to MgO and Mg_2SiO_4 phases were observed in addition to the reflection from the Mg substrate. The presence of Mg peaks at 2θ values of 32.2°, 34.4, 36.6°, 57.4° and 70.0° suggests that the coating is relatively thin and the X-ray could penetrate deep into the substrate. In the higher thickness coatings B-15 and C-15, an increase of intensity of MgO peaks at 42.9°and evolution of a new peak at 62.3° were observed. Further, the Mg_2SiO_4 peaks were evidently distinct with their higher intensities in these two specimens compared to the A-15 specimen.

Electrochemical Studies

Impedance measurements

The Bode plots from the EIS analysis are presented in **Figure 6**. The behaviour of the untreated AM50 alloy exhibited a distinctly different behaviour compared to that of the PEO coated specimens. The EIS data of the untreated magnesium substrate was fitted with a model consisting of a solution resistance (R_s), charge transfer resistance (R_t) and capacitance (C_{dl}), as described in the literature, and the resistance (R_t) was found to be around 1000 $\Omega \cdot cm^{-2}$. The EIS data of the PEO coated specimens were fitted with a widely accepted model for coatings, **(Figure 7) [5, 17]** and the derived electrochemical parameters are given in **Table 1**. Constant phase elements (CPE) were used in the electrochemical circuit instead of simple capacitors in order to account for the surface heterogeneity and diffusion factors. The admittance of CPE is expressed as:

$$Z_{CPE} = 1/ [T(j\omega)^P]$$

where T is the CPE constant, j is the imaginary unit ($j^2 = -1$), ω is the angular frequency ($rad \cdot s^{-1}$) and P is the CPE exponent. Depending on the value of P, CPE can represent resistance when P = 0, capacitance when P = 1 and Warburg impedance when P = 0.5.

It is evident from these impedance plots that these three coatings have different corrosion resistance/behaviour. The effective polarisation resistance is extremely high as the apparent area of exposure through the pores is very small for the PEO coated specimens. The data from curve fitting clearly suggest that the coatings produced at higher current density levels (B-15 and C-15) have a low resistance (R_p), which is attributed to the large sized pores and connecting pore channels in these coatings. Also, the inner layer/interface resistance R_f of the A-15 specimen was observed to be much higher than those of the B-15 and C-15 specimens. A closer look at the cross-section of the coatings in Figure 2 clearly reveals that the A-15 coating is more compact

compared to the other two. The seepage of electrolyte into the substrate though the micro-cracks, pores in the mid-section and also near the coating/substrate interface is responsible for the inferior general corrosion resistance observed in the B-15 and C-15 specimens.

Potentiodynamic polarisation

The potentiodynamic polarisation behaviour of the untreated AM50 alloy and the PEO coated specimens are depicted in **Figure 8**, and the electrochemical data are presented in **Table 2**. The untreated specimen had exhibited a corrosion current density of 2.5 x 10^{-2} mA·cm^{-2} with an associated corrosion potential of -1452 mV vs. Ag/AgCl. The corrosion potentials of the A-15 PEO coated specimen was similar to that of the untreated specimen and the coatings produced at higher current density showed more active corrosion potentials. The corrosion current density values of the PEO coated specimens were better by 2-3 orders of magnitude than those of the untreated alloy and as was observed in the impedance measurements, the corrosion current density of the coating obtained at the low current density condition was lower, reaffirming its superior corrosion resistance. However, it is interesting to note that the breakdown potential of the A-15 specimen, which depicts the localised damage, was -1347 mV vs. Ag/AgCl and that of the B-15 and C-15 specimens were -1234 mV and -1322 mV, respectively. It may be expected that the thicker coatings give rise to better resistance to localised damage; however, as the defect level in the C-15 coating was quite significant, this specimen had registered a lower breakdown potential compared to that of B-15. Incidentally, this potential was found to be nearly the same as that for the A-15 specimen, suggesting that for a better localised corrosion resistance the coating needs to be not only thicker, but should be free from defects as well.

Short duration PEO processing at high current density

As the PEO coatings from the high current density operations did not provide a good corrosion resistance despite a higher coating thickness, it was decided to perform treatments at 150 mA·cm^{-2} for short durations and characterize the resultant coatings. As described in the coating evolution section, the coating formation rate was quite rapid at this current density level, and the 4^{th} stage was reached within 1 min. Hence, the PEO process was interrupted at 2 minutes (C-2) and 5 minutes (C-5) to get the short duration coatings. **Figures 9(a) and (b)** show the cross-section of the C-2 and C-5 specimens, and the corresponding scanning electron micrographs showing the morphological features are depicted in **Figures 10(a) and (b)**. The interfaces of these

two coatings appear to be very similar to the A, B, C specimens discussed in the earlier sections. In terms of porosity level and compactness, these coatings resemble more those of the A-15 specimen. The surface morphologies, however, are different and these coatings seem to contain quite a few larger pores in addition to the smaller ones when compared to the A-15 specimen. Between the C-2 and C-5 specimens, the discernable difference is in the form of chunks of deposits in the latter case. Thickness measurements showed average values of 13 µm and 20 µm for the C-2 and C-5 specimens respectively, with corresponding average surface roughness values of 0.75 µm and 1.30 µm. From the thickness data, it can be seen that the average growth rates were 6.5 µm/min, 4 µm/min and 3 µm/min for the C2, C5 and C15 specimens, and this suggests that the coating formation is very high in the initial stages and it slows down as the process proceeds.

The electrochemical behaviour of the C-2 and C-5 specimens examined by EIS is presented in **Figure 11** and the results are documented in **Table 3**. The R_p and R_f values of the C-2 specimen were nearly similar to those of the A-15 specimen, which also had a similar coating thickness. The higher degree of porosity could have been responsible for the marginal differences. On the other hand, the resistance values of the C-5 specimen were again close to those of the B-15 specimen. Even though the thickness of the C-5 coating was lower than B-15, the compactness of the coating would have been the reason for the on par corrosion behaviour registered. The potentiodynamic polarisation behaviour of the C-2 and C-5 specimens presented in **Figure 12** and **Table 4** also had a similar trend as discussed above, with the C-2 and C-5 specimens showing a performance similar to the A-15 and B-15 counterparts. These observations clearly suggest that the short term PEO treatments at higher current density levels could be very helpful for increasing the productivity of processing without compromising much on the corrosion resistance.

Conclusions

1. The growth of coatings is influenced significantly by the operating current density in PEO processing. Average growth rates of 1 µm/min, 2 µm/min and 3 µm/min were registered at 15 $mA{\cdot}cm^{-2}$, 75 $mA{\cdot}cm^{-2}$, and 150 $mA{\cdot}cm^{-2}$ conditions, respectively.

2. The thickness, roughness and porosity/defect levels of the coatings increase with increase in current density for a given processing duration.

3. Relatively thin coatings with a higher degree of compactness obtained from low current density PEO operations offer a superior corrosion resistance as evidenced in the short term EIS and polarisation tests.

4. The interrupted short duration PEO experiments at 150 $mA \cdot cm^{-2}$ showed that the coating growth rate was very high in the first two stages of processing and it slowed down in the last two stages. The trend was very similar in the other two current density levels, too.

5. Short duration PEO treatments at higher current density levels yield coatings of comparable thickness and corrosion resistance as obtained for low current density operations. Short term treatments at higher current density levels help in improving the productivity of PEO processing.

Acknowledgement

The authors thank the AvH Foundation, Germany and DAAD, Germany for the award of research fellowships to PBS and JL. The technical support of Mr. Ulrich Burmester and Mr. Volker Heitmann during the course of this work is gratefully acknowledged.

References

1. J.D. Gray, B. Luan: Journal of Alloys and Compounds, 336 (2002), 88.

2. C. Blawert, V. Heitman, W. Dietzel, M. Stoermer, Y. Bohne, S. Maendl, B. Rauschenbach, Materials Science Forum, 539-543 (2007) 1679.

3. H. Zhao, Z. Huang, J. Cui: Microelectronics Engineering, 85 (2008) 253.

4. C. Blawert, V. Heitmann, W. Dietzel, H.M. Nykyforchyn, M.D. Klapkiv: Surface and Coatings Technology, 201 (2007) 8709.

5. S. Sathiyanarayanan, S. Azim, G. Venkatachari, Applied Surface Science, 253 (2006) 2113

6. Y. Zhang, C. Yan, F. Wang, H. Lou, C. Cao, Surface and Coatings Technology, 161 (2002) 36.

7. H.G. Guo, M.Z. An, Applied Surface Science, 246 (2005) 229.

8. C. Blawert, W. Dietzel, E. Ghali, G. Song: Advanced Engineering Materials, 8 (2006) 511.

9. H. Luo, Q. Cai, B. Wei, B. Yu, D. Li, J. He, Z. Liu, Journal of Alloys and Compounds, 464 (2008) 537.

10. J. Liang, L. Hu, J. Hao, Applied Surface Science, 253 (2007) 4490.

11. R. Arrabal, E. Matykina, F. Viejo, P. Skeldon, G.E. Thompson, Corrosion Science, 50 (2008) 1744.

12. Q. Cai, L. Wang, B. Wei, Q. Liu, Surface and Coatings Technology, 200 (2006) 3727.

13. J. Liang, L. Ju, J. Hao, Applied Surface Science, 253 (2007) 6939.

14. A.V. Timoshenko, Y.V. Magurova, Surface and Coatings Technology, 199 (2005) 135.

15. G.H. Lv, W.C. Gu, H. Chen, W.R. Feng, M.L. Kosha, L. Li, L. Niu, G.L. Zhang, S.Z. Yang, Applied Surface Science, 253 (2006) 2947.

16. G.H. Lv, H. Chen, W.C. Gu, L. Li, E.W. Niu, X.H. Zhang, S.Z. Yang, Journal of Materials Processing Technology, 208 (2008) 9.

17. A. Ghasemi, V.S. Raja, C. Blawert, W. Dietzel, K.U. Kainer, Surface and Coatings Technology, 202 (2008) 3513.

Table 1 Electrochemical fitting data for the PEO coated specimens from EIS

Designation	R_s, Ω·cm^2	$(CPE\text{-}T)_p$	$(CPE\text{-}P)_p$	R_p, Ω·cm^2	$(CPE\text{-}T)_f$	$(CPE\text{-}P)_f$	R_f, Ω·cm^2
A-15	18	5.89E-8	0.87	88000	1.52E-6	0.40	1.07E6
B-15	22	1.42E-7	0.81	43500	1.72E-6	0.41	3.57E5
C-15	22	1.04E-7	0.84	14600	2.79E-6	0.35	2.78E5

Table 2 Electrochemical data for the untreated and PEO coated specimens from potentiodynamic polarisation studies

Designation	E_{Corr}, mV vs. Ag/AgCl	I_{corr}, mA·cm^{-2}	E_{pit}, mV vs. Ag/AgCl
Untreated	-1452	2.5×10^{-2}	-1440
A-15	-1449	1.5×10^{-5}	-1347
B-15	-1472	5.3×10^{-5}	-1234
C-15	-1498	1.6×10^{-4}	-1322

Table 3 Electrochemical fitting data for the PEO coated specimens from EIS

Designation	R_s, Ω·cm^2	$(CPE\text{-}T)_p$	$(CPE\text{-}P)_p$	R_p, Ω·cm^2	$(CPE\text{-}T)_f$	$(CPE\text{-}P)_f$	R_f, Ω·cm^2
C-2	21	6.98E-8	0.87	84000	1.68E-6	0.42	9.50E5
C-5	19	7.50E-8	0.86	41750	1.43E-6	0.42	3.59E5
C-15	22	1.04E-7	0.84	14600	2.79E-6	0.35	2.78E5

Table 4 Electrochemical data for the PEO coated specimens from potentiodynamic polarisation studies

Designation	E_{Corr}, mV vs. Ag/AgCl	I_{corr}, mA·cm^{-2}	E_{pit}, mV vs. Ag/AgCl
C-2	-1436	2.4×10^{-5}	-1343
C-5	-1451	5.4×10^{-5}	-1301
C-15	-1498	1.6×10^{-4}	-1322

Figure Captions

Figure 1 Voltage vs. time plots obtained during PEO processing at different current densities

Figure 2 Scanning electron micrographs showing the cross-sections of the specimens PEO coated at different current densities for 15 minutes

Figure 3 Scanning electron micrographs showing the surface morphologies of the specimens PEO coated at different current densities for 15 minutes

Figure 4 Average thickness and roughness of the specimens PEO coated at different current densities for 15 minutes

Figure 5 X-ray diffraction patterns of the specimens PEO coated at different current densities for 15 minutes

Figure 6 EIS spectra (Bode plots) of the specimens PEO coated at different current densities for 15 minutes (test electrolyte: 0.1 M NaCl solution)

Figure 7 Electrochemical circuit employed for curve fitting
R_s – Solution resistance
R_p – Resistance of porous outer layer
R_f – Resistance of inner layer/interface
CPE_p– Constant phase element representing the porous outer layer
CPE_f – Constant phase element representing the inner layer/interface

Figure 8 Potentiodynamic polarisation behaviour of the specimens PEO coated at different current densities for 15 minutes (test electrolyte: 0.1 M NaCl solution)

Figure 9 Scanning electron micrographs showing the cross-section of specimens PEO coated at 150 $mA{\cdot}cm^{-2}$ (a) 2 minutes (b) 5 minutes

Figure 10 Scanning electron micrographs showing surface morphology of specimens PEO coated at 150 $mA{\cdot}cm^{-2}$ (a) 2 minutes (b) 5 minutes

Figure 11 EIS spectra (Bode plots) of the specimens PEO coated at 150 $mA{\cdot}cm^{-2}$ for different durations (test electrolyte: 0.1 M NaCl solution)

Figure 12 Potentiodynamic polarisation behaviour of the specimens PEO coated at 150 $mA{\cdot}cm^{-2}$ for different durations (test electrolyte: 0.1 M NaCl solution)

Figure 1
Click here to download high resolution image

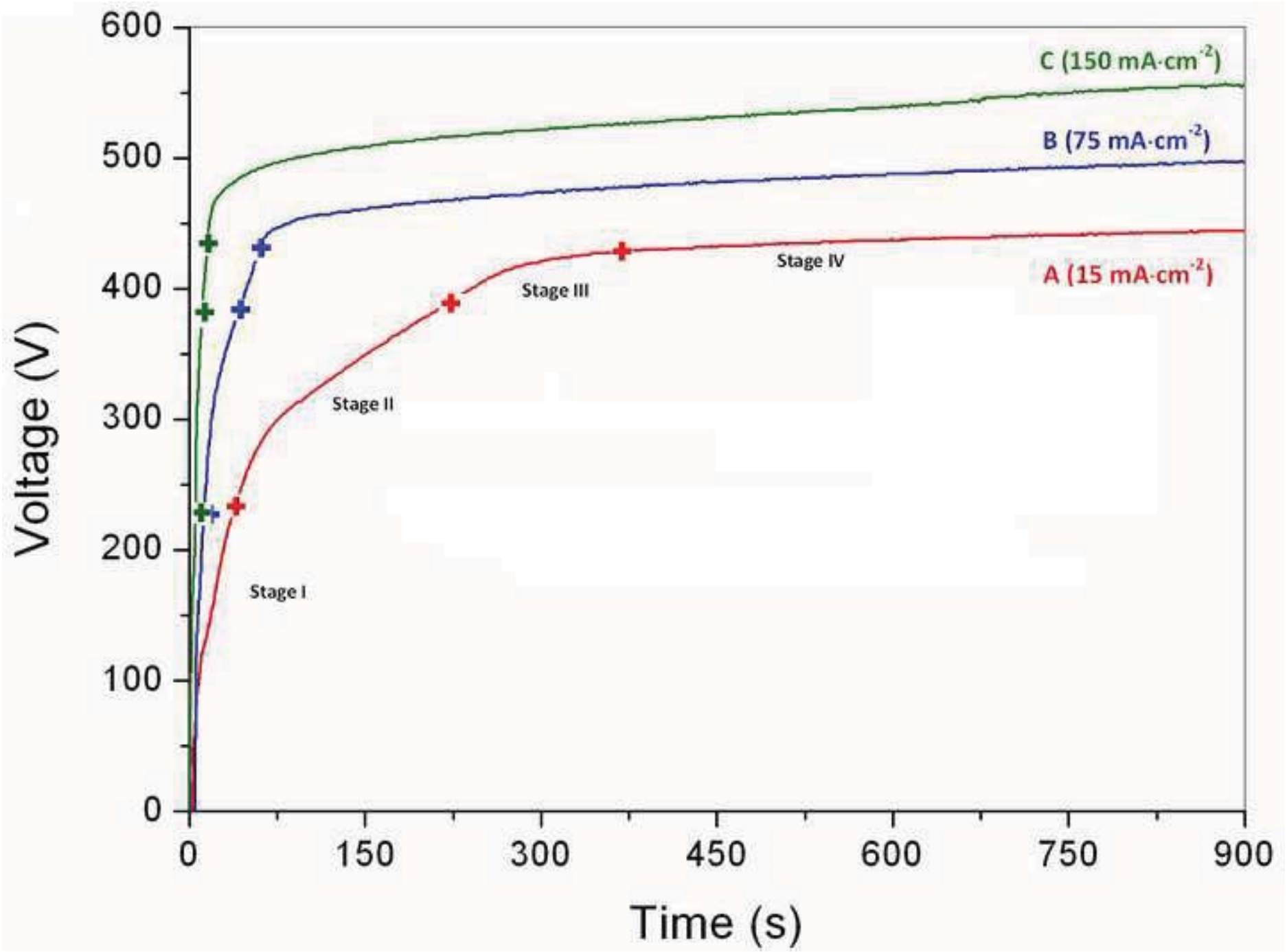

Figure 2a
Click here to download high resolution image

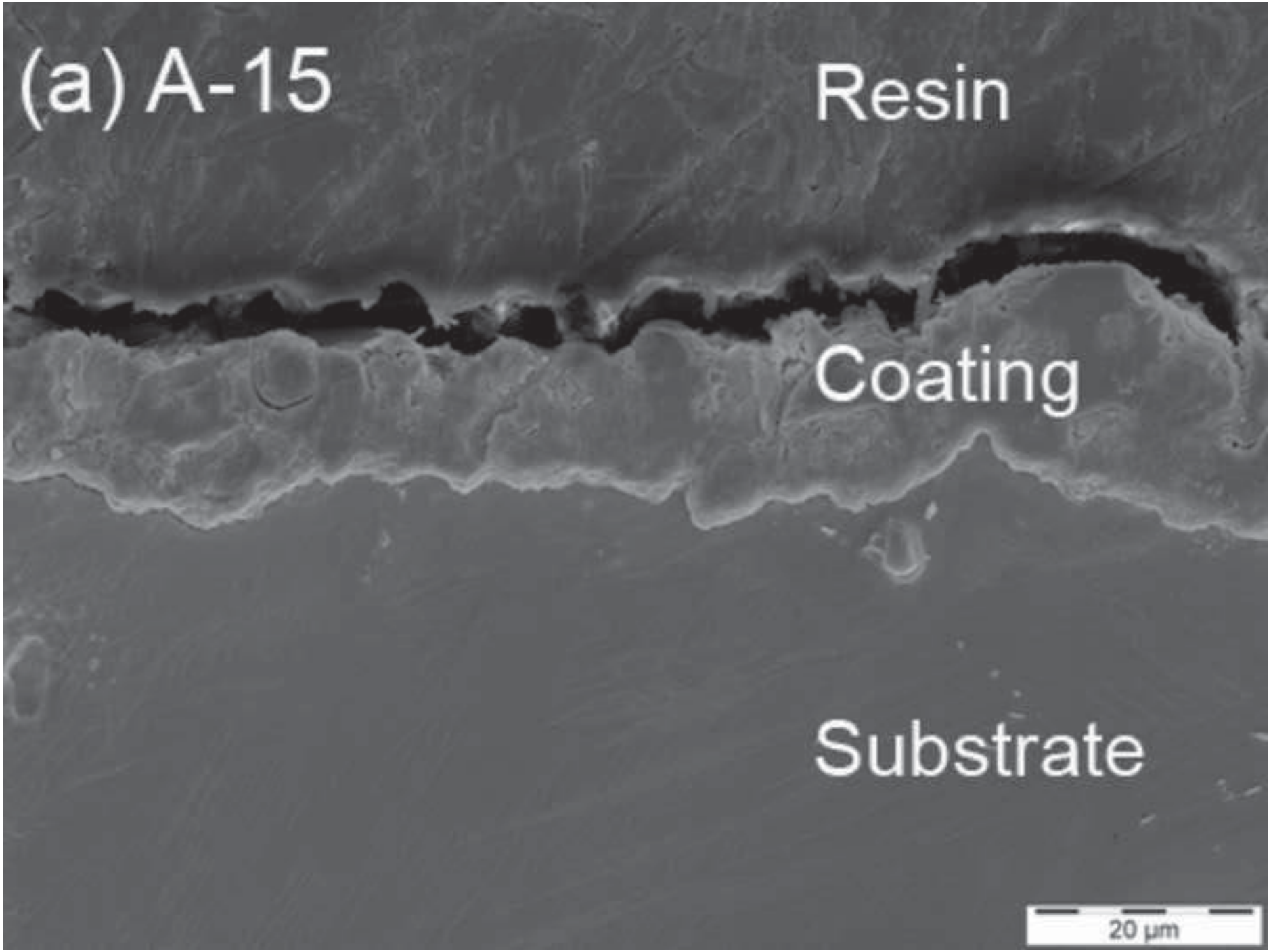

Figure 2b

Click here to download high resolution image

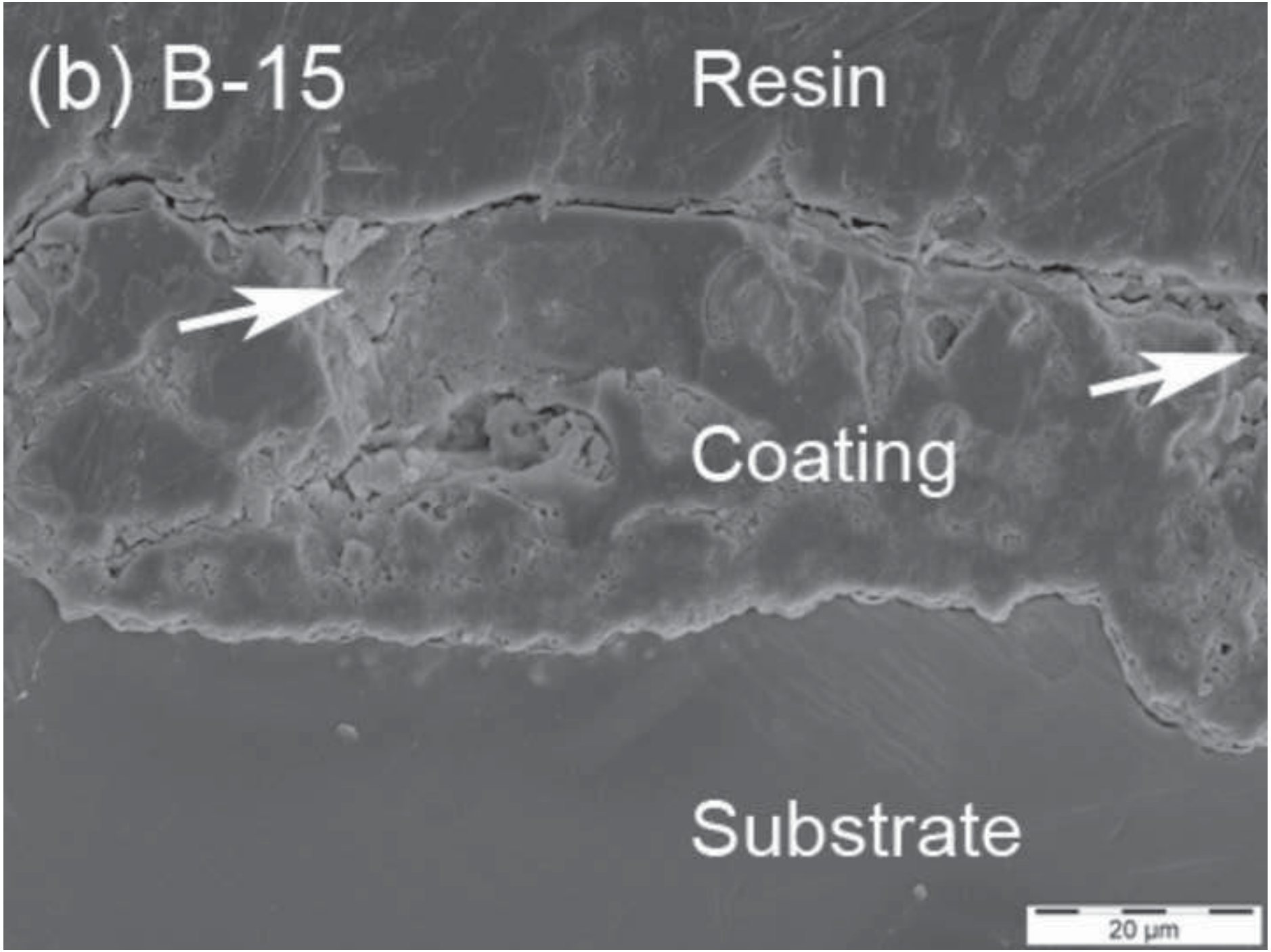

Figure 2c

Click here to download high resolution image

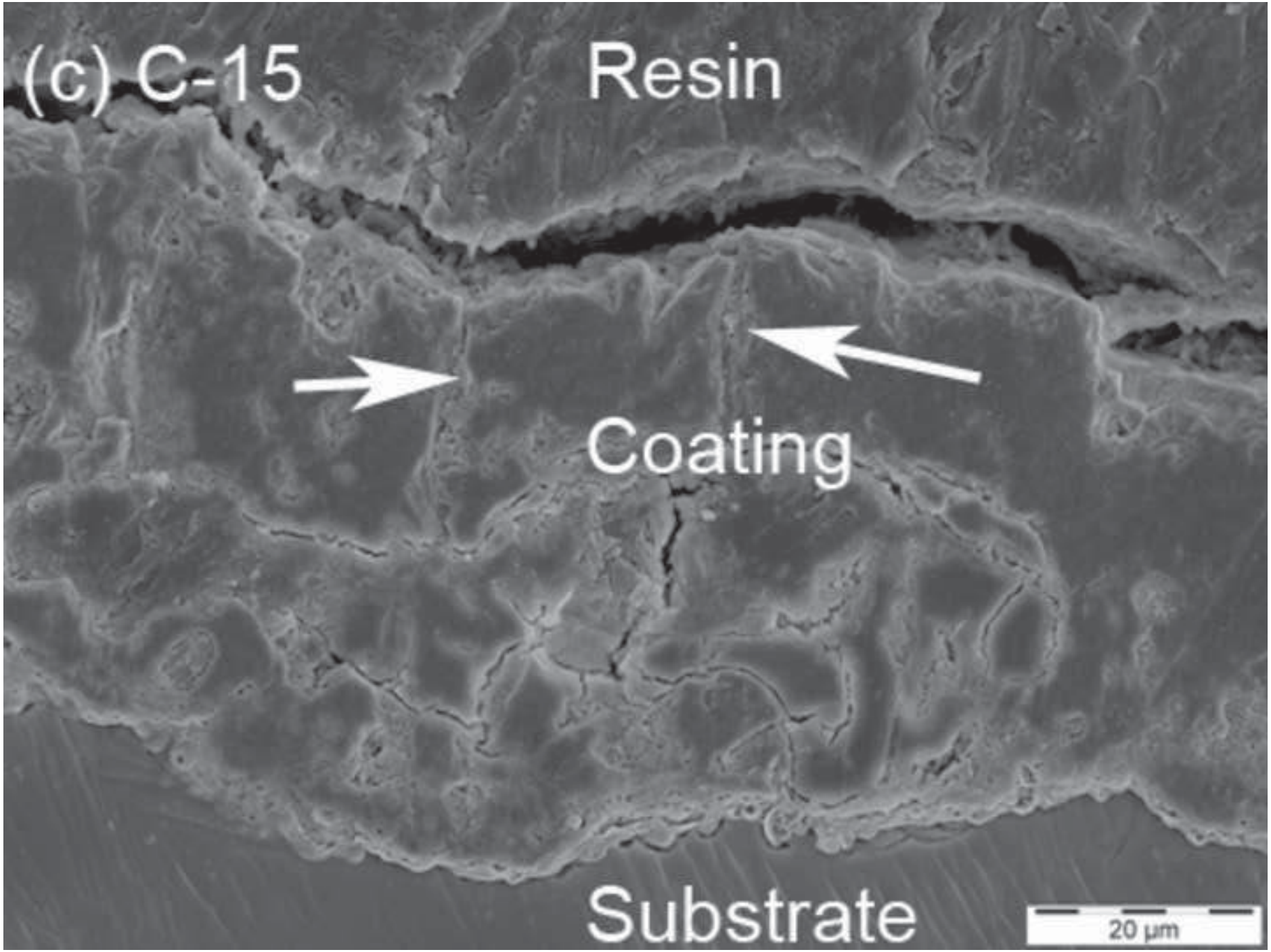

Figure 3a
Click here to download high resolution image

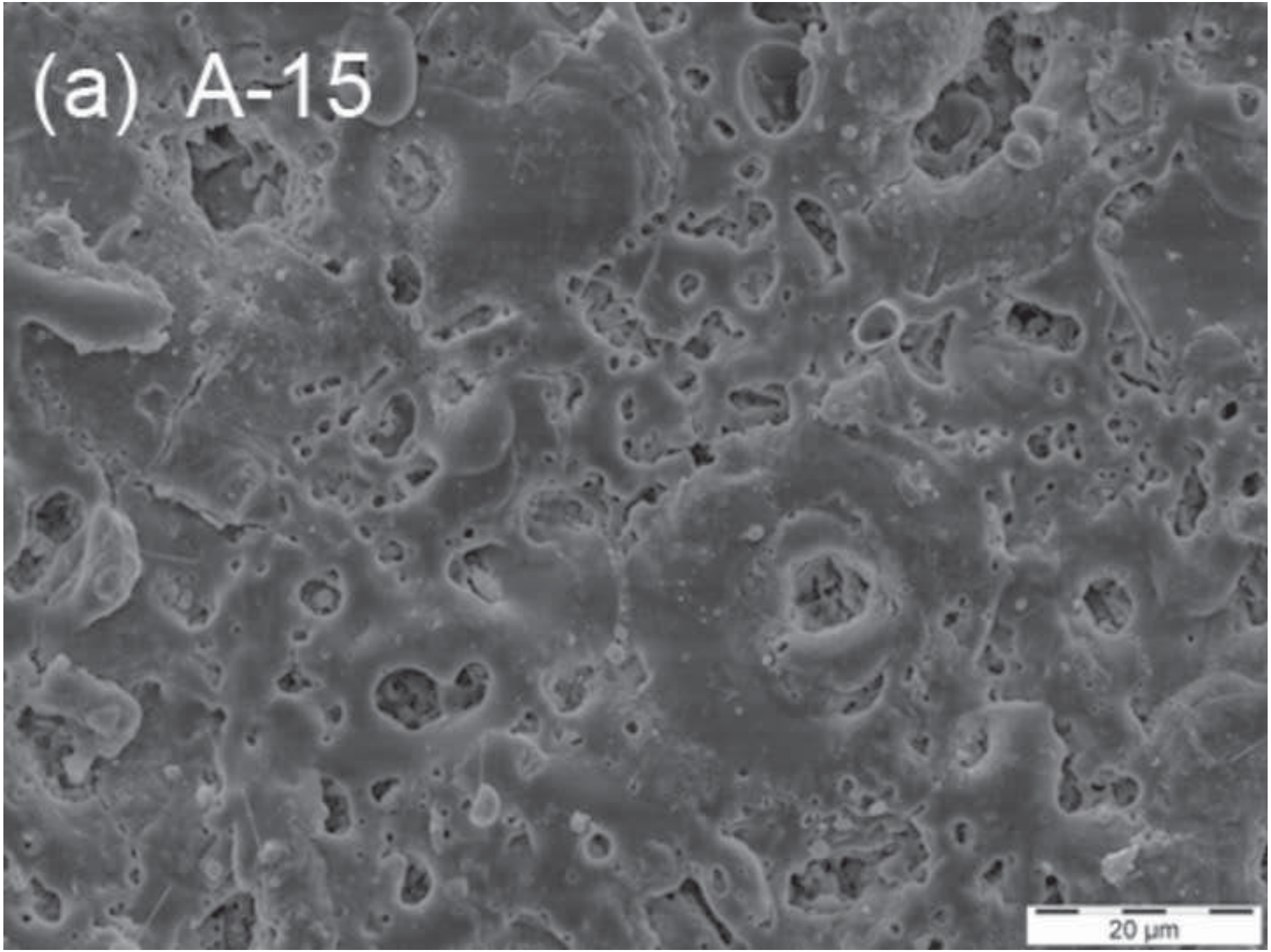

Figure 3b
Click here to download high resolution image

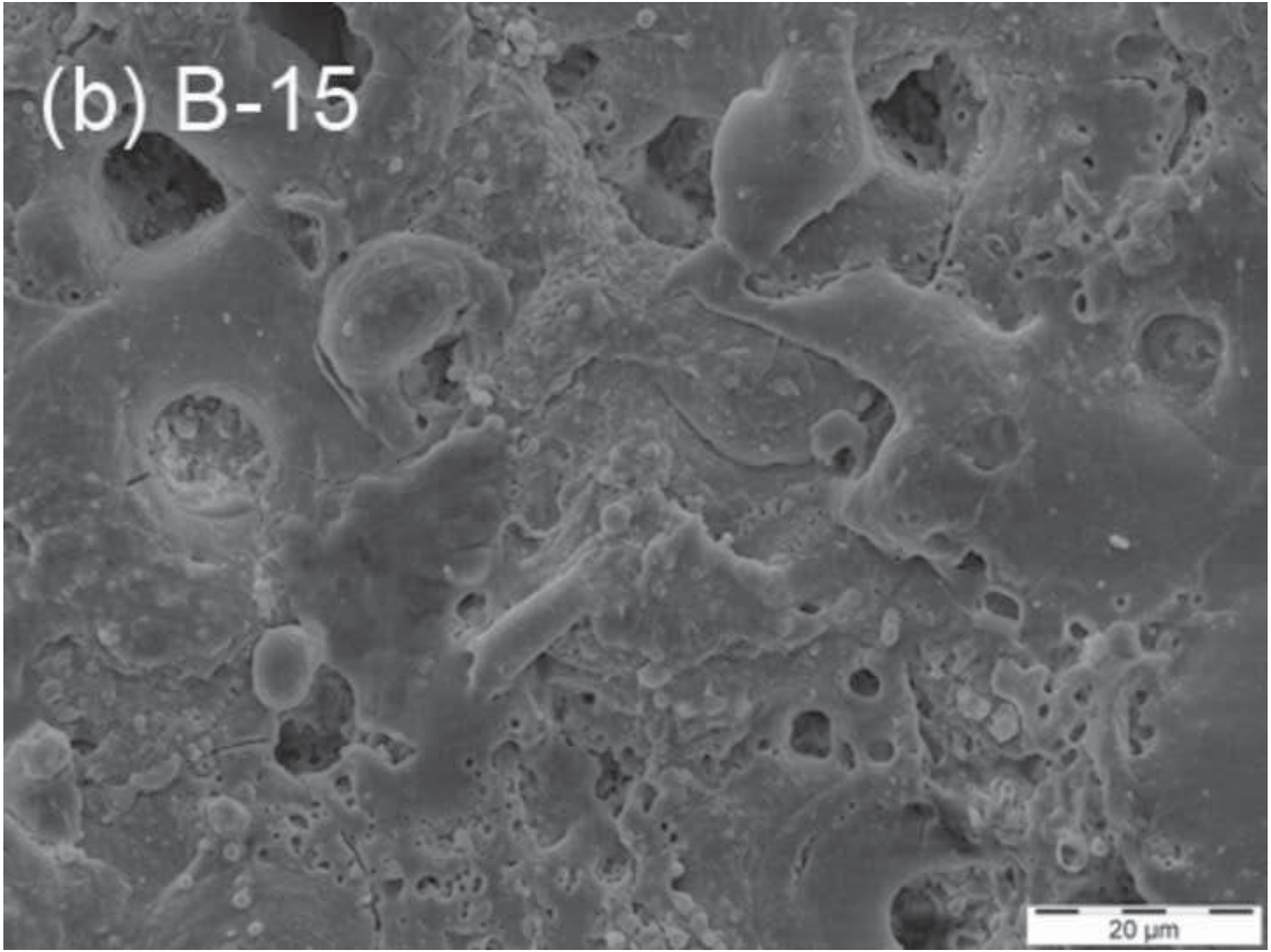

Figure 3c

Click here to download high resolution image

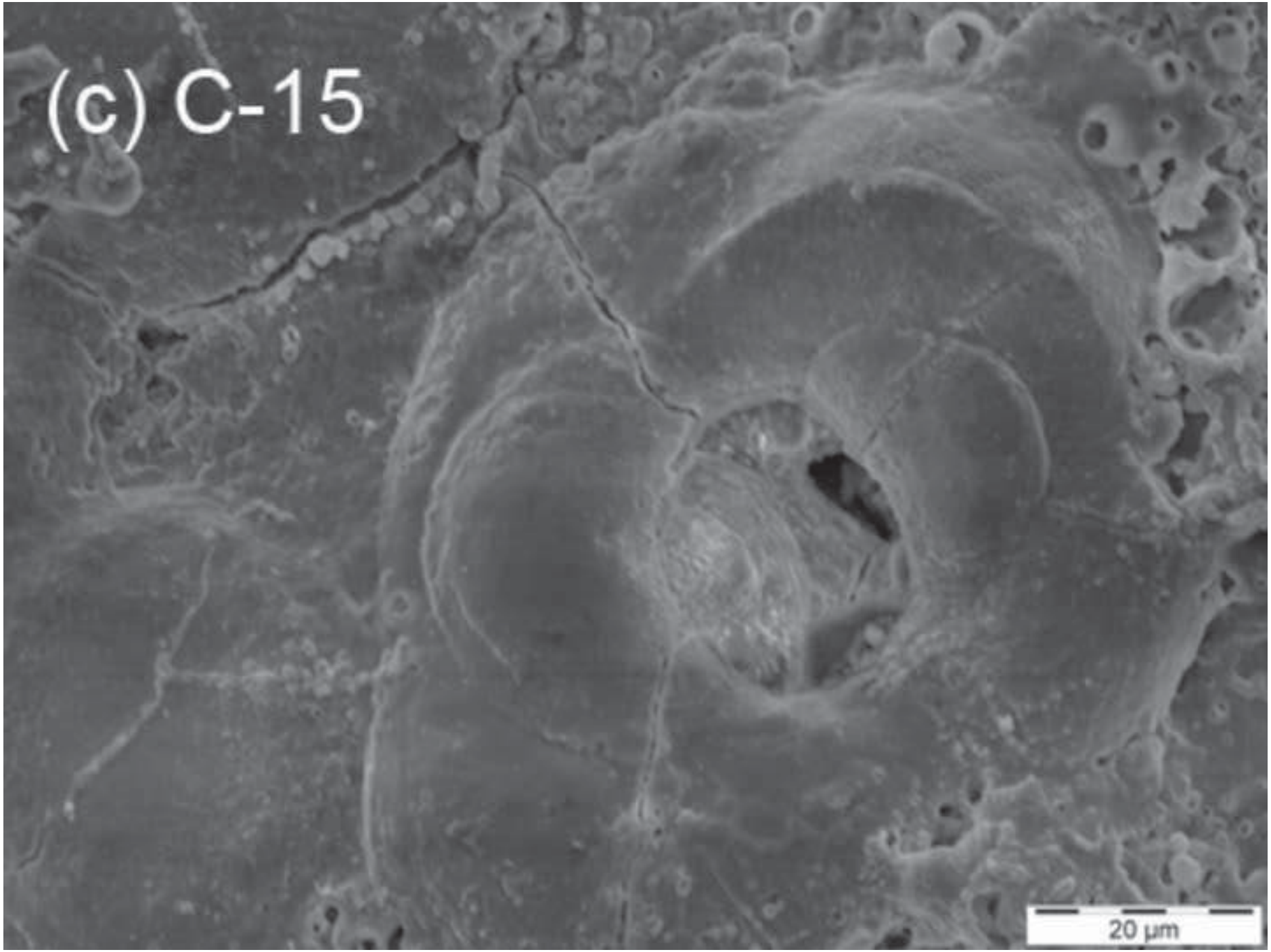

Figure 4
Click here to download high resolution image

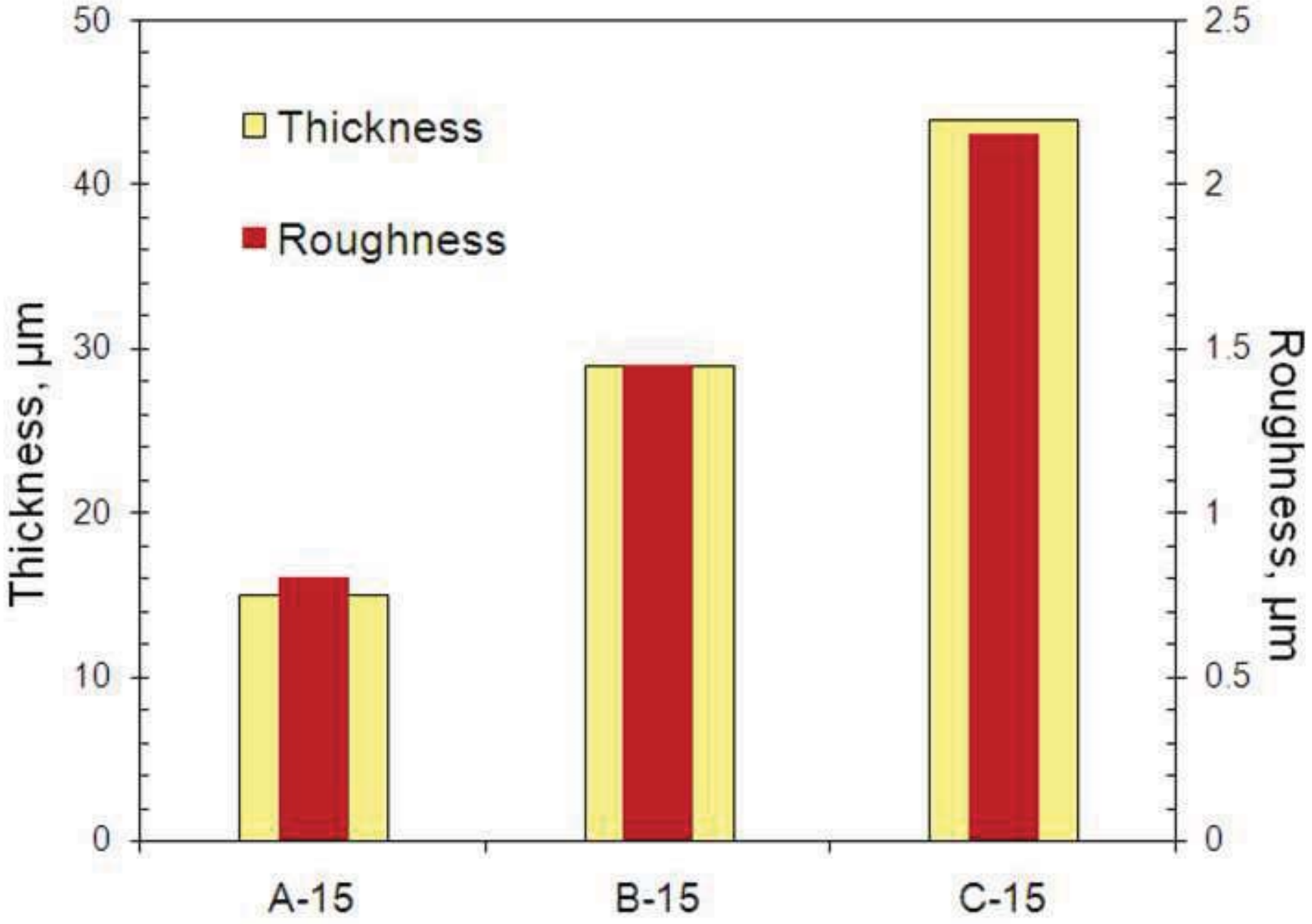

Figure 5
Click here to download high resolution image

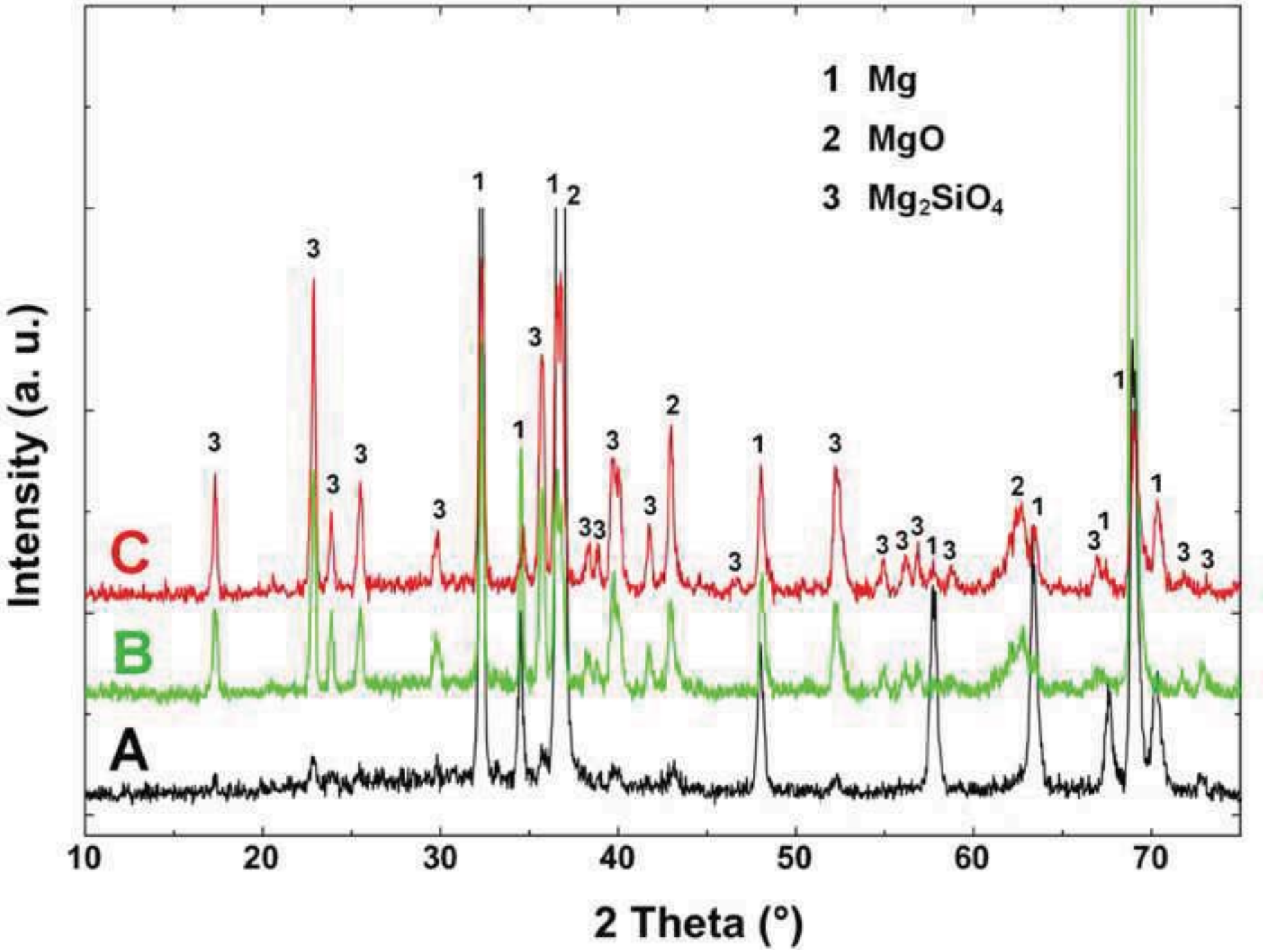

Figure 6

Click here to download high resolution image

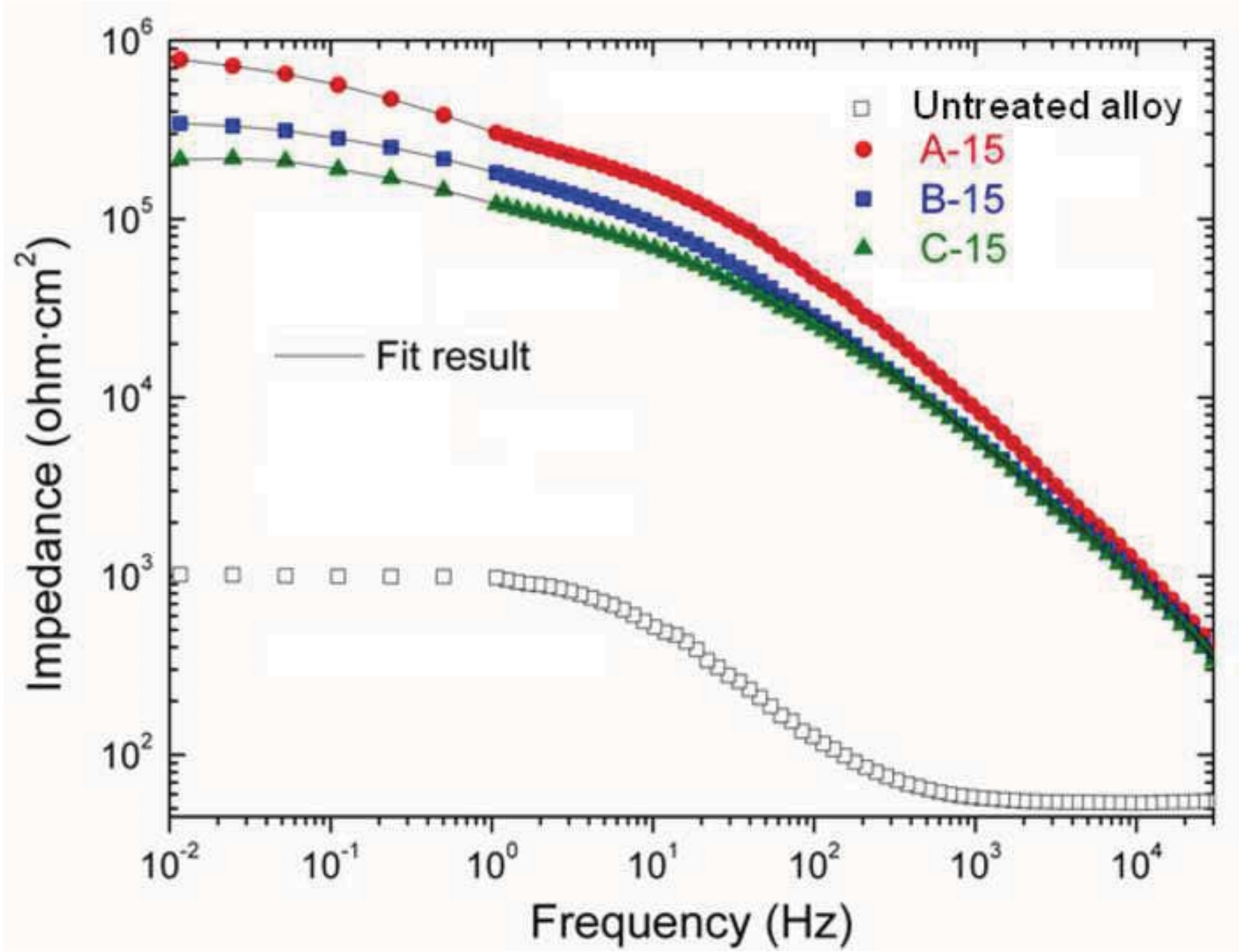

Figure 7
Click here to download high resolution image

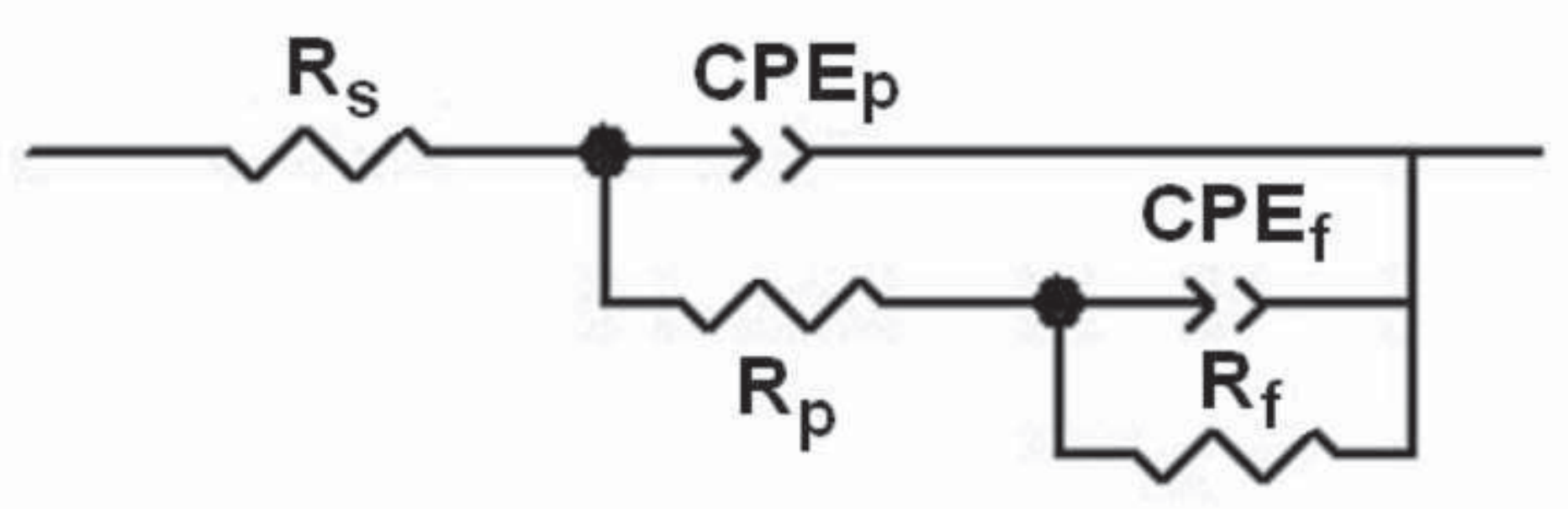

Figure 8
Click here to download high resolution image

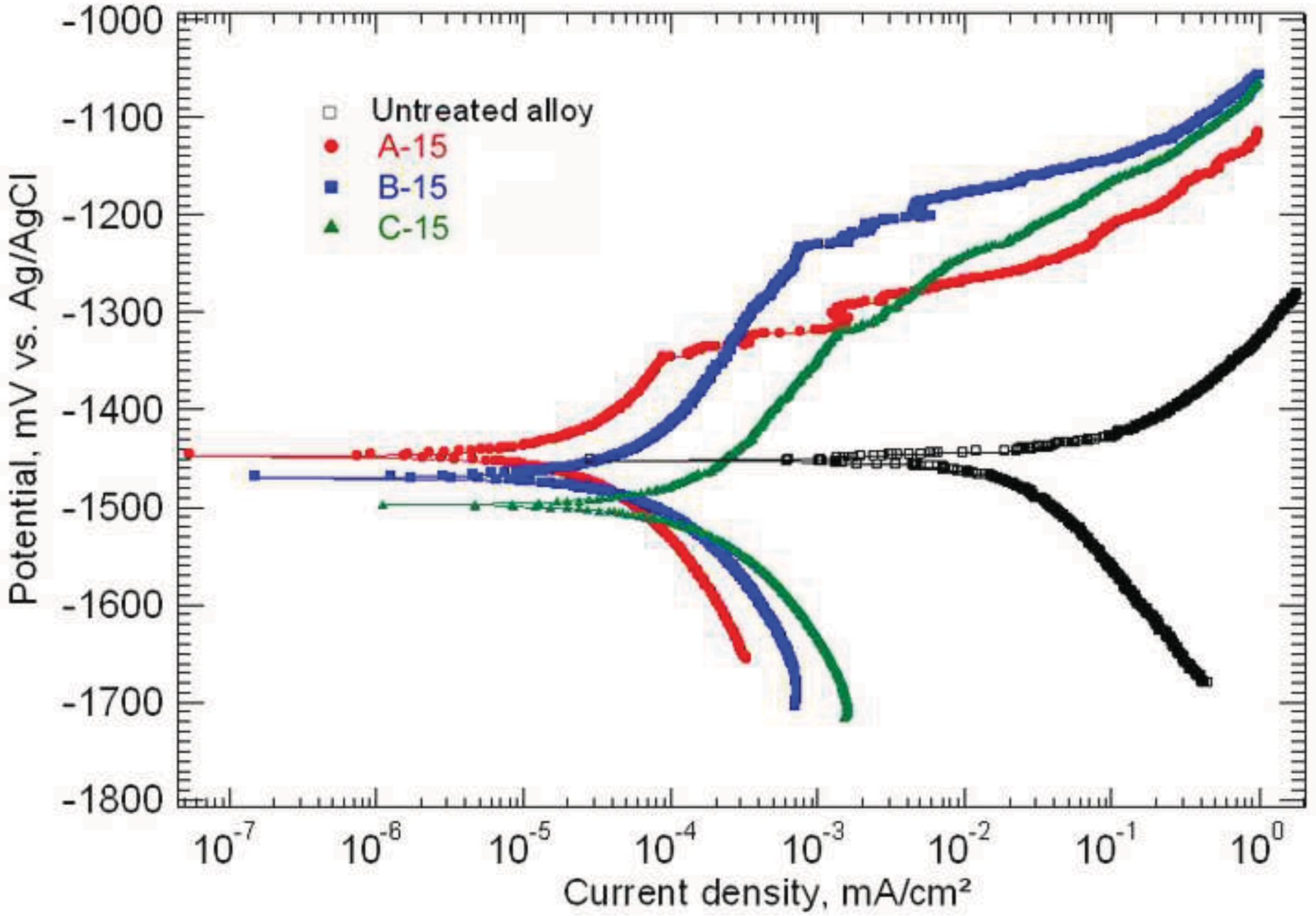

Figure 9a
Click here to download high resolution image

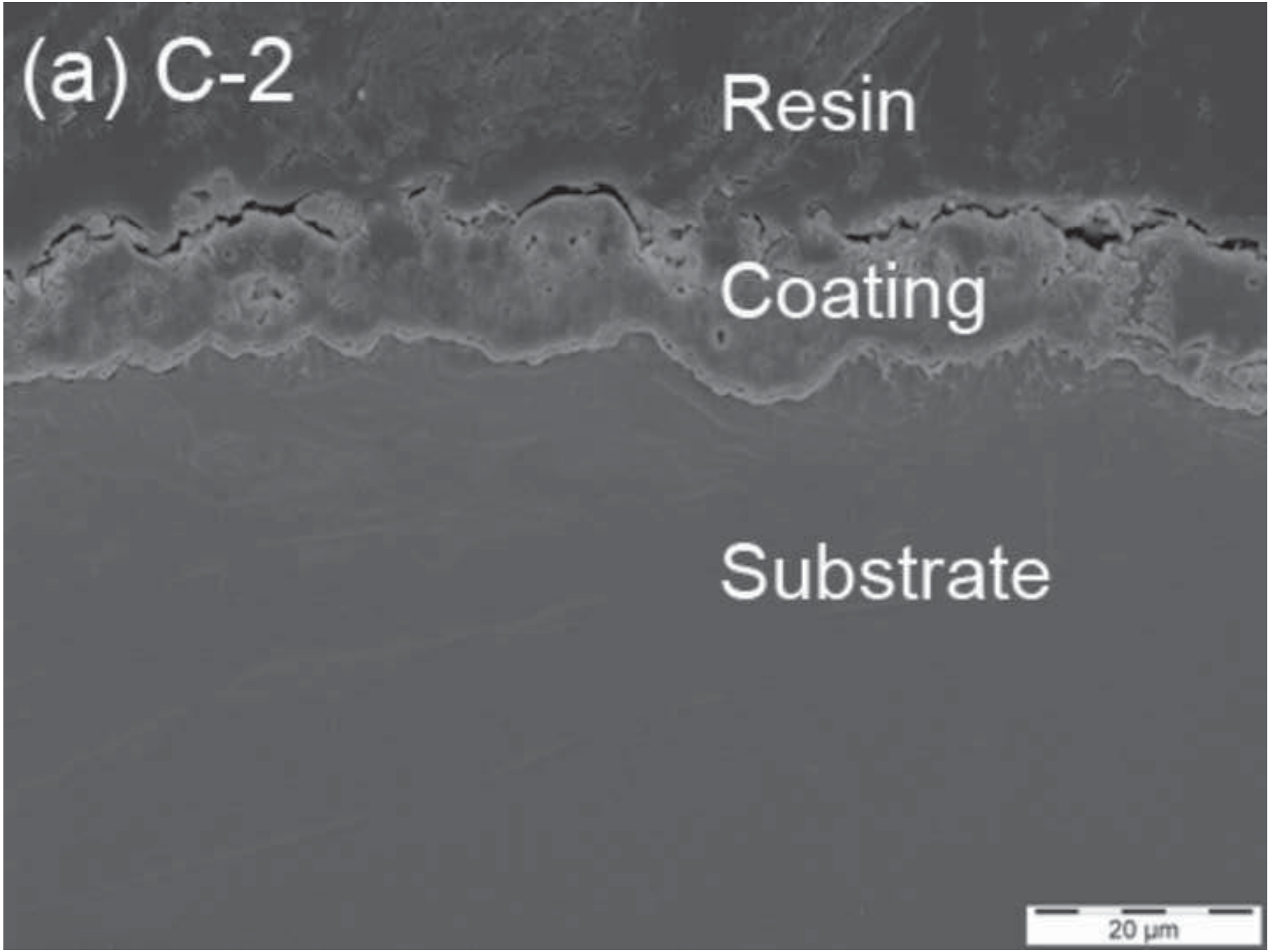

Figure 9b
Click here to download high resolution image

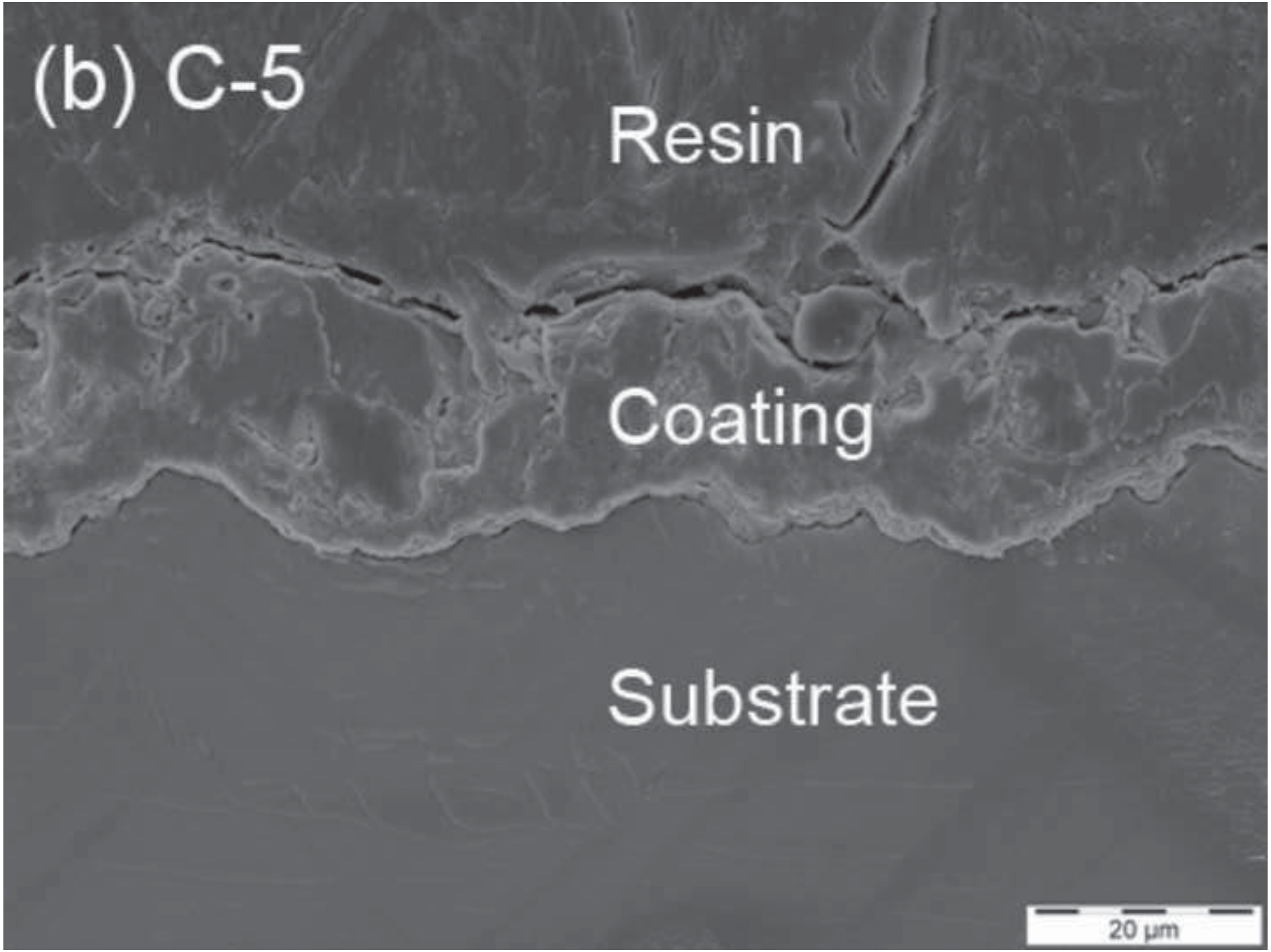

Figure 10a

Click here to download high resolution image

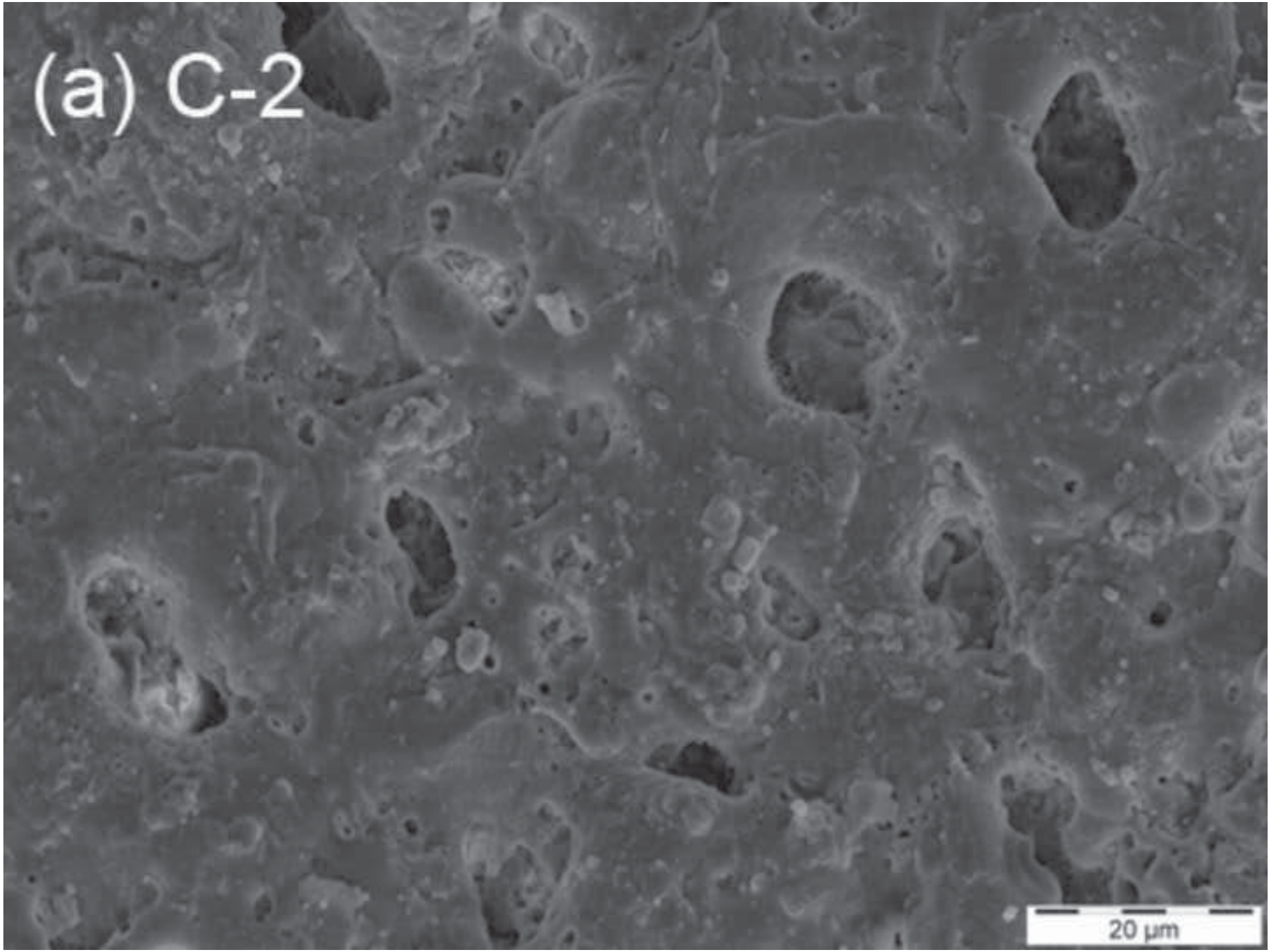

Figure 10b

Click here to download high resolution image

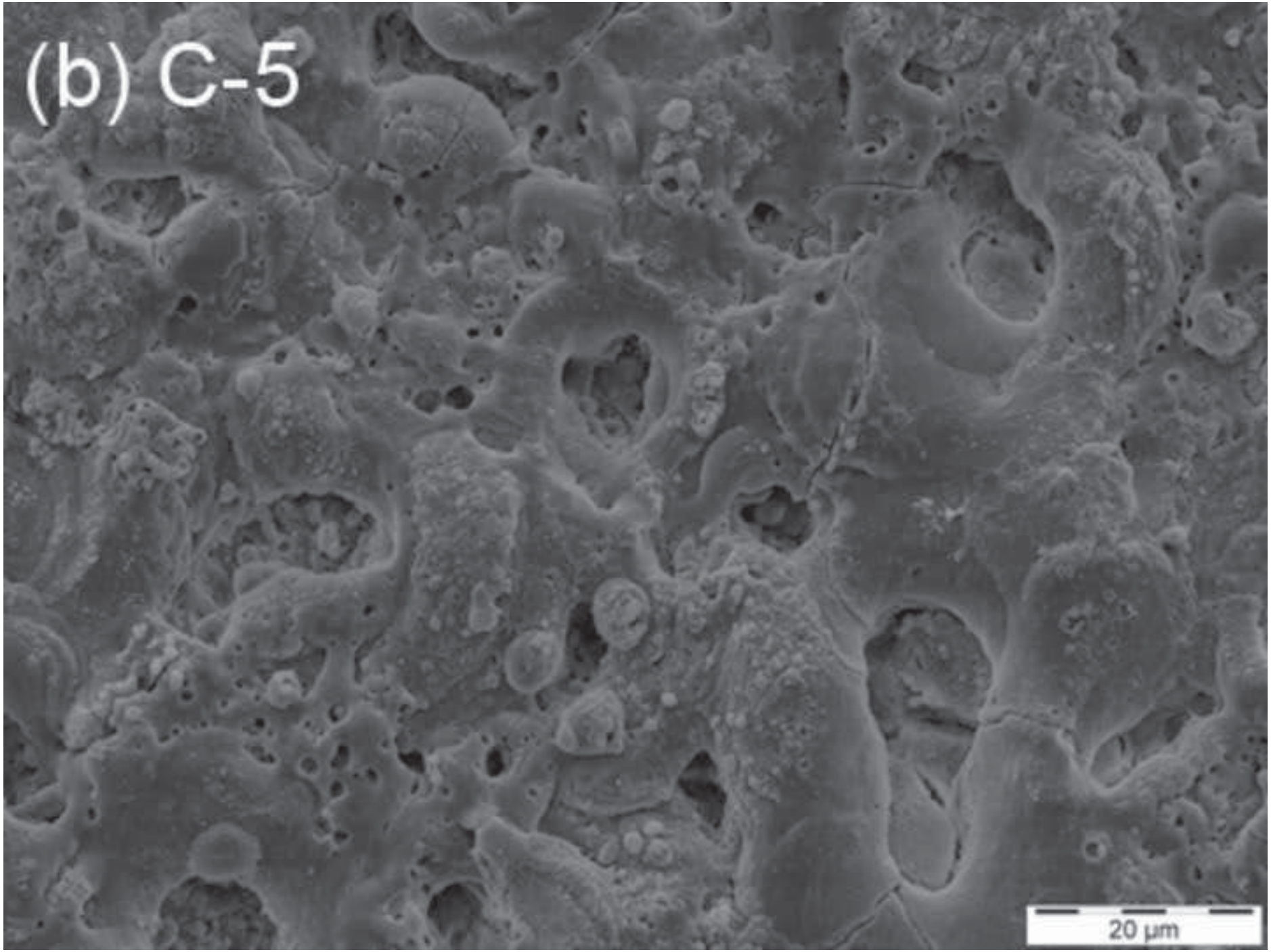

Figure 11
Click here to download high resolution image

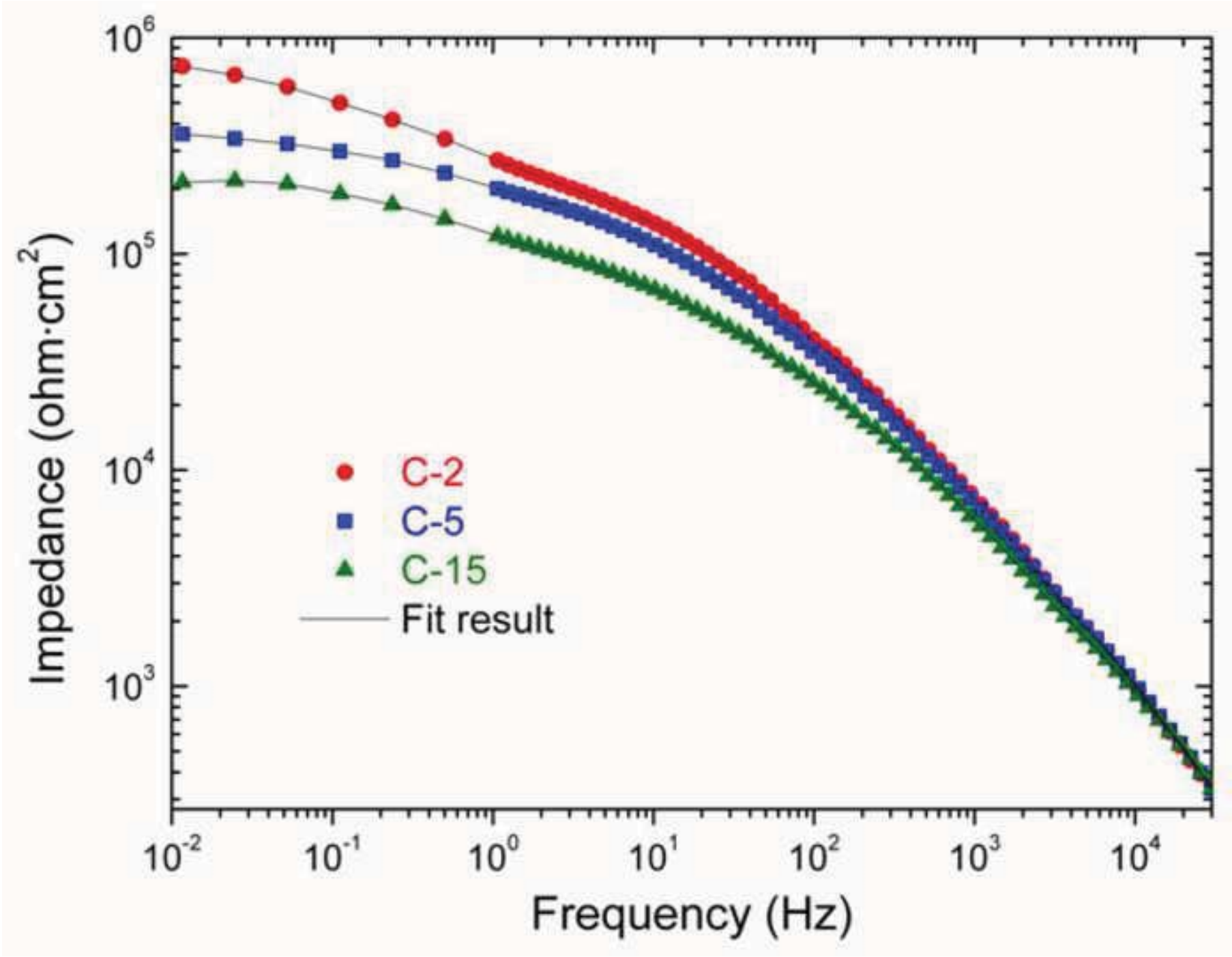

Figure 12
Click here to download high resolution image